Oxidation of aluminum nanoclusters

Timothy J. Campbell,[1,2] Gurcan Aral,[1] Shuji Ogata,[3] Rajiv K. Kalia,[1] Aiichiro Nakano,[1] and Priya Vashishta[1]
[1]*Collaboratory for Advanced Computing and Simulations, Department of Materials Science and Engineering, Department of Physics and Astronomy, Department of Computer Science, University of Southern California, Los Angeles, California 90089-0242, USA*
[2]*Mississippi State University, Stennis Space Center, Mississippi 39529, USA*
[3]*Graduate School of Engineering, Nagoya Institute of Technology, Nagoya 466-8555, Japan*
(Received 21 June 2004; published 26 May 2005)

The dynamics of oxidation of aluminum nanoclusters (20 nm diameter) is investigated using a parallel molecular dynamics approach based on variable charge interatomic interactions due to Streitz and Mintmire that include both ionic and covalent effects. Simulations are performed for both canonical ensembles for molecular oxygen (O_2) environments and microcanonical ensembles for molecular (O_2) and atomic (O_1) oxygen environments. Structural and dynamic correlations in the oxide region are calculated, as well as the evolution of charges, surface oxide thickness, diffusivities of atoms, and local stresses. In the microcanonical ensemble, the oxidizing reaction becomes explosive in both molecular and atomic oxygen environments due to the enormous energy release associated with Al-O bonding. Local stresses in the oxide scale cause rapid diffusion of aluminum and oxygen atoms. Analyses of the oxide scale reveal significant charge transfer and a variation of local structures from the metal-oxide interface to the oxide-environment interface. In the canonical ensemble, oxide depth grows linearly in time until ~30 ps, followed by saturation of oxide depth as a function of time. An amorphous oxide layer of thickness ~40 Å is formed after 466 ps, in good agreement with experiments. The average mass density in the oxide scale is 75% of the bulk alumina density. Evolution of structural correlation in the oxide is analyzed through radial distribution and bond angles. Through detailed analyses of the trajectories of O atoms and their formation of OAl_n structures, we propose a three-step process of oxidative percolation that explains deceleration of oxide growth in the canonical ensemble.

DOI: 10.1103/PhysRevB.71.205413 PACS number(s): 61.46.+w, 81.05.Bx, 81.65.Mq

I. INTRODUCTION

A great deal of recent research has focused on the role of ultrafine microstructures in the physical and chemical behavior of materials synthesized from nanometer size clusters.[1–6] These nanophase materials have a large fraction of atoms in the interfacial regions, which has a dramatic effect on the structure and physical properties.[3,7,8] The mechanical strength of nanophase metals is known to be higher than that of conventional polycrystalline metals of the same chemical composition.[9] It has been predicted that nanophase ceramics are much more ductile and have lower sintering temperatures than conventional brittle ceramics.[10–12]

A particularly interesting possibility is the synthesis of nanocomposites consisting of metallic nanoclusters coated with a passivation layer. Upon compaction, the passivation layer forms a boundary layer between the isolated metallic grains, and the resulting passivating network has a dramatic effect on the electrical, chemical, and mechanical behavior. In a study by Sánchez-López *et al.*,[13] Al/Al-oxide nanocomposites were found to have a metallic shine and an Ohmic electrical resistivity. The nanocomposite consisted of 300 Å aluminum particles with an interconnected 40 Å oxide layer that prevented the material from falling apart above the aluminum melting temperature. Other studies indicate that the properties of these nanocomposite materials are strongly dependent on the nature of the passivation layer.[14–16]

A few experimental studies of the passivation behavior of ultrafine Al particles have been reported in recent years. NMR measurements[15] reveal that 500–700-Å-sized Al particles form a 25–50-Å-thick oxide scale when exposed to air. The oxide scale remains intact, even after compacting the Al nanopowders at high pressures. Thermogravimetric studies show that a 200-Å Al cluster forms an oxide scale with a thickness of 30–40 Å.[16] Aumann *et al.*[17] have studied the oxidation of Al nanopowders for raising the ignition threshold of highly reactive ultrafine grain Al/MoO_3 powders. They observed that powders consisting of Al particles with diameters between 240 and 650 Å oxidize with a square-root time dependence similar to flat Al samples. They also found that the increased surface area of Al particles lowers the oxidizing activation energy relative to that of flat Al samples. More recent studies by Sánchez-López[14] on the passivation of Al nanoclusters show that for the range of particle sizes studied (120–410 Å) the oxide scale thickness ~40 Å is independent of oxygen dosage. Experiments indicate that the structure of the oxide scale on Al nanoclusters is amorphous, but there exists no detailed structural analysis. Recent studies have suggested that the structure of the amorphous oxide scale of Al nanoclusters is different from that of the amorphous scale on the bulk Al surface.[14,17]

Experimentally, the growth of oxide scales on bulk metallic surfaces exhibits several types of behavior. Theoretical study of the oxidation of bulk metal surfaces was pioneered by Wagner,[18] Mott,[19] and Cabrera and Mott.[20] The oxidation rate depends on the temperature and access of oxygen to the metal atoms. A linear rate of oxidation occurs when the oxide is porous and the metal surface is continually exposed to oxygen.[21] This behavior is typical of metals such as magne-

sium, in which the oxide occupies a small volume fraction of the metal. The resulting tensile stresses cause the oxide film to crack and become porous. Oxide growth exhibits either square root or logarithmic time dependence, when the controlling factor is the diffusion of ions or electrons through a nonporous oxide layer. Examples are Al, Cr, Ni, and Ti. As for Al, the logarithmic growth is observed at temperatures below ~700 K, while the square root growth is observed at higher temperatures.[22] It has been inferred from experimental studies of scale morphology and the behavior of impurity markers that Al_2O_3 grows by inward migration of oxygen at high temperatures.[22] Grain boundary diffusion of oxygen is considered as the most likely migration process controlling the growth of Al_2O_3 scales.[22]

In this paper we report the results of a large-scale, parallel molecular dynamics (MD) simulation of the oxidation of an Al nanocluster (diameter 200 Å). We have investigated the structural and dynamic correlations in the oxide region and the evolution of charge, surface oxide thickness, diffusivities of atoms, and local stresses. The MD simulations are based on the ES+ model of Streitz and Mintmire,[23] which takes into account the effect of charge transfer between Al and O using the electronegativity equalization principle. The organization of the paper is as follows. Section II describes the simulation method and schedule, and results are given in Sec. III. Finally, Sec. IV contains conclusions.

II. COMPUTATIONAL METHODS

A. MD simulation method

In the MD simulation technique, the dynamical history of an ensemble of atoms (phase-space trajectory) is computed from Newton's equations of motion. Hence, we are able to observe the time evolution of microscopic phenomena. Additionally, based on different statistical ensemble, macroscopic physical properties can be obtained from this detailed information using statistical mechanics by sampling on different phase-space surfaces. Each statistical ensemble has its own conserved thermodynamic quantities such as energy (E), temperature (T), and pressure (P).

In conventional MD simulation, averages of physical quantities are measured in the microcanonical ensemble (*NVE*). We consider a system of N atoms with coordinates $\{\mathbf{r}_i: i=1,\ldots,N\}$ and momenta $\{\mathbf{p}_i: i=1,\ldots,N\}$ within a fixed volume V. The atoms are assumed to interact with a potential $\mathcal{V}=\mathcal{V}(\{\mathbf{r}_i\})$. Treating the atoms as classical pointlike objects the Hamiltonian of the system is written as

$$\mathcal{H}=\sum_{i=1}^{N}\frac{\mathbf{p}_i^2}{2m_i}+\mathcal{V}(\{\mathbf{r}_i\}), \tag{1}$$

where m_i is the mass of the ith atom in the system. Based on the Hamilton equations of motion,

$$\mathbf{r}_i=\frac{\partial\mathcal{H}}{\partial\mathbf{p}_i},\quad \mathbf{p}_i=-\frac{\partial\mathcal{H}}{\partial\mathbf{r}_i}, \tag{2}$$

the Newton equations of motion are reduced from Hamiltonian (1)

$$m_i\ddot{\mathbf{r}}_i=-\nabla_{\mathbf{r}_i}\mathcal{V}=\mathbf{f}_i,\quad i=1,\ldots,N \tag{3}$$

where $\mathbf{f}_i$ is the force on atom i. The most important input information in MD simulations is the expression for the potential energy. Given an initial configuration $\{\mathbf{r}_i(0),\mathbf{p}_i(0)\}$, the set of $3N$ coupled second-order differential equations in (3) are numerically integrated in time to generate the dynamical history of the system.

In order to simulate other statistical ensembles, additional variables are introduced into the Lagrangian to represent the coupling of the system with external sources. In the canonical ensemble (*NVT*), the system is thermally coupled with a heat reservoir. The canonical ensemble was first introduced in MD simulations by Nosé.[24,25] Starting with the extended Hamiltonian

$$\mathcal{H}_{Nosé}=\sum_{i=1}^{N}\frac{\mathbf{p}_i^2}{2m_is^2}+\mathcal{V}(\{\mathbf{r}_i\})+\frac{p_s^2}{2Q}+(3N+1)k_BT\ln s, \tag{4}$$

where Q is the "mass" associated with the variable s, Nosé showed that microcanonical distribution for the extended system is equivalent to the canonical distribution of the set of variables $\{\mathbf{r}_i,\mathbf{p}_i/s\}$. The variable s is interpreted as a time scaling factor, where the time in the canonical distribution is related to the real time as $2t'=t/s$. A slightly different representation that is free of the time scaling was later developed by Hoover,[26] who showed that the equations of motion of Nosé are in fact unique and therefore the two representations are equivalent. Martyna *et al.*[27] extended the Nosé-Hoover dynamics to employ a chain of thermostats by proposing the following conserved quantity for the system:

$$\mathcal{H}=\sum_{i=1}^{N}\frac{\mathbf{p}_i^2}{2m_i}+\sum_{i=1}^{M}\frac{p_{\xi_i}^2}{2Q_i}+\mathcal{V}(\{\mathbf{r}_i\})+3Nk_BT\xi_1+k_BT\sum_{i=2}^{M}\xi_i, \tag{5}$$

where M is the number of thermostats ξ_j, and Q_j and p_{ξ_j} are, respectively, the mass and momenta of thermostat ξ_j.

B. Interatomic potential with variable charge transfer

The underpinning of MD simulations is the interatomic potential. The quality of the simulation results are determined by the accuracy of the potential, and the amount of compute time is determined by its functional complexity. The MD simulations of oxidation of aluminum nanoclusters are based on an interaction model developed by Streitz and Mintmire[23] that can successfully describe a wide range of physical properties of Al and Al_2O_3. This so-called electrostatic plus (ES+) model is capable of treating (i) both metallic and ceramic systems, (ii) bond formation and bond breakage, and (iii) changes in charge transfer as the atoms move and their local environments are constantly altered. In the ES+ model, the potential energy of the system is expressed as the sum of an electrostatic potential (ES) and an embedded-atom potential: $\mathcal{V}(\{\mathbf{r}_i,q_i\})=\mathcal{V}_{\mathrm{EAM}}(\{\mathbf{r}_i\})+\mathcal{V}_{\mathrm{ES}}(\{\mathbf{r}_i,q_i\})$.

The potential in the embedded atom method (EAM) is defined as

$$\mathcal{V}_{EAM} = \sum_i \mathcal{F}_i[\rho_i] + \sum_{i<j} \phi_{ij}(r_{ij}), \tag{6}$$

where $\mathcal{F}_i[\rho_i]$ represents the energy required to embed atom i in a local electron density ρ_i and $\phi_{ij}(r_{ij})$ is an additional pairwise interaction, with r_{ij} the interatomic distance between atoms i and j. In the ES+ model a Finnis-Sinclair[28] form is chosen for the embedding energy

$$\mathcal{F}_i[\rho_i] = -A_i\sqrt{\rho_i/\xi_i}, \tag{7}$$

where

$$\rho_i(r) = \sum_{j\neq i} \xi_j \exp[-\beta_j(r_{ij} - r_j^*)]. \tag{8}$$

In Eq. (8) the local atomic density ρ_i is expressed as a linear superposition of atomic densities of all other atoms. The pairwise potential is chosen to be

$$\phi_{ij}(r) = 2\beta_{ij}\exp\left[-\frac{\beta_{ij}}{2}(r - r_{ij}^*)\right] - C_{ij}[1 + \alpha(r - r_{ij}^*)]\exp[-\alpha(r - r_{ij}^*)]. \tag{9}$$

The total electrostatic energy $\mathcal{V}_{\mathrm{ES}}(\mathbf{r},q)$ is a function of the atomic charges (valence) and positions in order to determine the local atomic charge from the local environment of each atom

$$V_{ES} = \sum_i \nu_i(q_i) + \frac{1}{2}\sum_{i\neq j} \nu_{ij}(\mathbf{r}_{ij};q_i,q_j),$$

$$\nu_i(q_i) = \nu_i(0) + \chi_i^0 q_i + \frac{1}{2}J_i^0 q_i^2,$$

$$\nu_{ij}(\mathbf{r}_{ij};q_i,q_j) = \int d^3r_1 \int d^3r_2 \rho_i(\mathbf{r}_1;q_i)\rho_j(\mathbf{r}_2;q_j)/r_{12}. \tag{10}$$

The local atomic energy $\nu_i(q_i)$ is a second-order Taylor expansion in the partial charge q_i. The first derivative χ is the electronegativity[29] and the second derivative J is associated with self-Coulomb repulsion.[30] The Coulomb interaction $\nu_{ij}(\mathbf{r}_{ij};q_i,q_j)$ in Eq. (10) represents the electrostatic interaction energy between atoms i and j. The function $\rho_i(\mathbf{r};q_i)$ represents the charge-density distribution about an atom i (including the nuclear point charge) for a total charge q_i. For mathematical convenience, Streitz and Mintmire chose a distribution, ρ_i, that is an extended form of a Slater-type 1s orbital

$$\rho_i(\mathbf{r};q_i) = \mathcal{Z}_i\delta(\mathbf{r} - \mathbf{r}_i) + (q_i + \mathcal{Z}_i)\left(\frac{\zeta_i^3}{\pi}\right)\exp(-2\zeta_i|\mathbf{r} - \mathbf{r}_i|), \tag{11}$$

where ζ_i is the decay length for atomic orbitals and $\mathcal{Z}_i$ is an effective core charge ($0<\mathcal{Z}_i<Z_i$, with Z_i the total nuclear charge of an atom). Applying Eqs. (10) and (11) together with the two-center Coulomb integrals[31] yields an expression for the electrostatic energy

$$\mathcal{V}_{ES} = \sum_i q_i\left\{\chi_i^0 + \sum_{j\neq i}\mathcal{Z}_j[\omega_i(r_{ij}) - \upsilon_{ij}(r_{ij})]\right\} + \frac{1}{2}\sum_i q_i^2 J_i^0 + \frac{1}{2}\sum_{j\neq i} q_i q_j\left[\frac{1}{r_{ij}} + \upsilon_{ij}(r_{ij})\right], \tag{12}$$

where $\upsilon_{ij}(r)$ is the short-range Coulomb-interaction integral and $\omega_j(r_{ij})$ is the short-range nuclear-attraction integral. Note that the electrostatic energy Eq. (12) contains a long-range Coulomb interaction term. As a result, the most time consuming part of ES+ potential is the long-range Coulomb interactions. The resulting Coulomb interaction is calculated with the $O(N)$ fast multipole method (FMM).[32]

The parameters in the ES+ potential are fitted to the bulk properties of both fcc aluminum and α-alumina crystal structures. In addition, the potential yields reasonable surface energies and relaxations for several low-index surfaces of α-alumina.

The unique feature of the ES+ model potential is that it explicitly includes dynamic charge transfer between anions and cations. The method is based on a semiempirical approach, in which atomic charges are determined according to the electronegativity equalization condition.[30,33–35] The ES+ model potential for TiO_2 systems has also been constructed,[36] which reproduces various quantities including dielectric constants of both rutile (ground state) and anatase phases with high accuracies. Such high transferability of the potential makes it possible to successfully perform sintering simulations of TiO_2 nanoparticles.[37,38]

In MD simulations, the atomic charges, q_i, are determined at each time step by minimizing the electrostatic energy [Eq. (12)], subject to the charge-neutrality constraint, $\Sigma_i q_i = 0$. This constrained minimization is algebraically equivalent to the electronegativity equalization condition that the chemical potentials $\partial\mathcal{V}_{\mathrm{ES}}/\partial q_i$ be equal for all atoms. This leads to a set of linear equations for atomic charges $\{q_i\}$

$$\sum_j M_{ij}q_j = \mu - \chi_i, \tag{13}$$

where M_{ij} is the Coulomb-interaction matrix and μ is a Lagrange multiplier used to determine the charge-neutrality constraint. In practice, the solution to Eq. (13) involves concurrent solution of two sets of linear equations. This minimization is equivalent to solving these two linear equation systems. Accordingly, the computational cost of the variable-charge MD scales as $O(N^3)$. To reduce that complexity to $O(N)$, we have developed several algorithms.

We use a conjugate gradient (CG) method[39] to solve these two linear systems. We have developed an acceleration scheme that computes the matrix-vector multiplication, $\Sigma_j M_{ij}q_j$, in $O(N)$ time using the FMM. Also the charges, $\{q_i\}$, determined at the previous MD step are used to initialize an iterative solution to Eq. (13), reducing the number of iterations to $O(1)$ and thus the total computational cost to determine atomic charges is linear in N.

To further speed up the solution of this minimization problem, our multilevel preconditioned conjugate gradient (MPCG) method splits the Coulomb-interaction matrix into

short- and long-range components: $M=M_s+M_l$,[40] thereby accelerating the solution. The preconditioning scheme is found to substantially improve the convergence and parallel efficiency by increasing data locality. The MPCG algorithm has enabled a successful large-scale oxidation simulation.

An alternative approach to the earlier variable charge method is to treat the atomic charges as dynamic variables in an extended Lagrangian.[35] We also implemented the ES+ method using an extended Lagrangian scheme, in which charges are given fictitious masses and velocities and then propagated with the atomic degrees of freedom by Newton's equations of motion. Typically, the time step for the charge degree of freedom is much smaller than the time step for the atomic motion. Multiple time step integration schemes can be applied to speed up the computations.[41]

C. Long range force calculation by FMM

Molecular dynamics simulations for complex physical systems, such as oxidation of aluminum, can be computationally very demanding: they may require large numbers of atoms, long simulation times, and computationally intensive interatomic interactions. The most compute-intensive part of ES+ potential is the long-range Coulomb interactions. Therefore, long-range interactions present a major computational challenge in MD simulations. In the presence of periodic boundary conditions (pbc), the total Coulomb energy of a charge neutral system of N atoms is given by

$$\mathcal{V}=\frac{1}{2}\sum_{i=1}^{N}\sum_{j=1}^{N}\sum_{\mathbf{n}}{}'\frac{q_iq_j}{|\mathbf{r}_i-\mathbf{r}_j-\mathbf{n}|} \tag{14}$$

where q_i is the charge of atom i. The simple cubic lattice translation vector is $\mathbf{n}=(n_xL_x,n_yL_y,n_zL_z)$, where the L_α are the side lengths of the central MD cell. The prime on the sum over $\mathbf{n}$ implies that terms with $i=j$ are omitted when $\mathbf{n}=0$. Direct computation of (14) requires $O(N^2)$ operations, which is clearly intractable for the large N required for realistic simulations. Recently, the FMM, developed by Greengard and Rokhlin,[32,42] has been successfully used to rapidly accelerate the calculation of the long-range pairwise interactions in a large ensemble of sources in a single cell without pbc. In N particle simulations involving long-range interactions, the FMM reduces the number of computations required to evaluate all pairwise interactions from $O(N^2)$ to $O(N)$ with predictable error bounds. The FMM is based on the multipole expansion of the Coulomb interaction. The rapid decay of the multipole expansion enables one to calculate the Coulomb interaction efficiently for a specific level of precision.

In this part, we briefly summarize equations that we use in the present implementation[43] of the FMM. The motivation in multipole translation is to formulate a far-field representation for a collection of charges about some point in space and then to translate the result to a different point. Given a unit charge $\{q_i\}$ at a point $\mathbf{x}'=(r',\theta',\phi')$ in polar coordinates, the potential induced by that charge at $\mathbf{x}=(r,\theta,\phi)$ is given by[44]

$$\frac{1}{|\mathbf{x}-\mathbf{x}'|}=\sum_{n=0}^{\infty}\sum_{m=-n}^{n}\frac{r_<^n}{r_>^{n+1}}Y_n^{-m}(\theta',\phi')Y_n^m(\theta,\phi), \tag{15}$$

where $r_<=\min(r,r')$, $r_>=\max(r,r')$, and the functions Y_n^m are the spherical harmonics. The Y_n^m used in this discussion are defined from the associated Legendre polynomials

$$Y_n^m(\theta,\phi)=\left\{\begin{matrix}(-1)^m, m\geqslant 0\\ 1, m<0\end{matrix}\right\}\sqrt{\frac{(n-m)!}{(n+m)!}}P_n^m(\cos\theta)e^{im\phi},$$

$$P_n^m(x)\equiv\frac{1}{2^n n!}\frac{(n+m)!}{(n-m)!}(1-x^2)^{-m/2}\frac{d^{n-m}}{dx^{n-m}}(x^2-1)^n$$
$$(-n\leqslant m\leqslant n). \tag{16}$$

The rapid decay of expansion (15) in each of the defined domains allows the calculation of the Coulomb potential with a specified level of precision.

Now consider a collection of point charges $\{q_i,\mathbf{x}_i=(r_i,\theta_i,\phi_i):i=1,\ldots,N\}$ that are lying within a sphere of radius R centered at the origin. The electrostatic potential at a point $\mathbf{x}=(r,\theta,\phi)$ lying outside the sphere may be expressed in the form of a multipole expansion

$$\mathcal{V}(x)=\sum_{i=1}^{N}\frac{q_i}{|\mathbf{x}-\mathbf{x}_i|}=\sum_{n=0}^{\infty}\sum_{m=-n}^{n}\left\{\sum_{i=1}^{N}q_ir_i^nY_n^{-m}(\theta_i,\phi_i)\right\}\frac{Y_n^m(\theta,\phi)}{r^{n+1}}. \tag{17}$$

The form (17), called the far-field representation, is characterized by the set of outer multipole coefficients C_n^m defined by

$$C_n^m=\sum_{i=1}^{N}q_ir_i^nY_n^{-m}(\theta_i,\phi_i). \tag{18}$$

With the following definitions of outer functions O_n^m and inner functions I_n^m:

$$O_n^m(\mathbf{x})=O_n^m(r,\theta,\phi)=\frac{(-1)^n i^{|m|}}{A_n^m}\frac{Y_n^m(\theta,\phi)}{r^{n+1}}, \tag{19}$$

$$I_n^m(\mathbf{x})=I_n^m(r,\theta,\phi)=i^{-|m|}A_n^mr^nY_n^m(\theta,\phi), \tag{20}$$

where

$$A_n^m=A_n^{-m}=\frac{(-1)^n}{\sqrt{(n-m)!(n+m)!}}, \tag{21}$$

the translation theorem (15) can be rewritten as (for $r>r'$)

$$\frac{1}{|\mathbf{x}-\mathbf{x}'|}=\sum_{n=0}^{\infty}\sum_{m=-n}^{n}(-1)^nI_n^{-m}(\mathbf{x}')O_n^m(\mathbf{x}). \tag{22}$$

There are three basic transformation operations necessary to implement the FMM: the (i)outer-to-outer, (ii) outer-to-inner, and (iii) inner-to-inner transformations.[45] These operations will be defined and described in sequence; they are illustrated in Fig. 1. First we consider a set of point sources $\{q_i,\mathbf{x}_i=(r_i,\theta_i,\phi_i):\ i=1,\ldots,N\}$, located within a sphere S_0 of radius R_0 centered at $\mathbf{x}_0$ (i.e., $\mathbf{x}_i\in\{\mathbf{x}:|\mathbf{x}-\mathbf{x}_0|\leqslant R_0\}$). The ob-

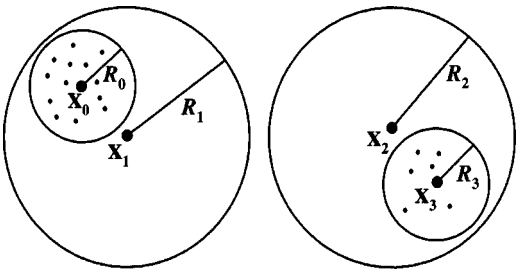

FIG. 1. Illustration of multipole transformation operations used in FMM for well separated sets of charges.

jective is to obtain an inner expansion for the potential due to the charges in sphere S_0 that is valid for points located in sphere S_3. The outer multipoles C_n^m that characterize the far-field representation (17) for this set of charges can be computed from (18). Then the potential at a point $\mathbf{x}$ outside the sphere S_0 is given by

$$\mathcal{V}(\mathbf{x}) = \sum_{n=0}^{\infty} \sum_{m=-n}^{n} C_n^m O_n^{-m}(\mathbf{x} - \mathbf{x}_0)$$

$$\mathbf{x} \notin \{\mathbf{x}: |\mathbf{x} - \mathbf{x}_0| \leqslant R_0\}. \tag{23}$$

We now consider a sphere S_1 that completely contains S_0 and desire to obtain a far-field representation for $\mathcal{V}(\mathbf{x})$ that is centered at $\mathbf{x}_1$ and is valid for $\mathbf{x}$ outside the sphere S_1. The outer-to-outer transformation that accomplishes this is given by

$$\mathcal{V}(\mathbf{x}) = \sum_{l=0}^{\infty} \sum_{j=-l}^{l} D_l^j O_l^{-j}(\mathbf{x} - \mathbf{x}_1), \tag{24}$$

where

$$D_l^j = \sum_{n=0}^{l} \sum_{m=-n}^{n} I_{l-n}^{j-m}(\mathbf{x}_1 - \mathbf{x}_0) C_n^m. \tag{25}$$

Suppose that sphere S_2 lies completely outside sphere S_1. The outer-to-inner transformation that gives a representation for $\mathcal{V}(\mathbf{x})$ valid for $\mathbf{x} \in \{\mathbf{x}: |\mathbf{x} - \mathbf{x}_2| \leqslant R_2\}$ is given by

$$\mathcal{V}(\mathbf{x}) = \sum_{l=0}^{\infty} \sum_{j=-l}^{l} E_l^j I_l^j(\mathbf{x} - \mathbf{x}_2), \tag{26}$$

where the inner multipole coefficients are given by

$$E_l^j = \sum_{n=0}^{\infty} \sum_{m=-n}^{n} O_{n+l}^{-m-j}(\mathbf{x}_2 - \mathbf{x}_1) D_n^m. \tag{27}$$

The final transformation takes the inner expansion centered at $\mathbf{x}_2$ and translates it to an inner expansion centered at $\mathbf{x}_3$

$$\mathcal{V}(\mathbf{x}) = \sum_{l=0}^{\infty} \sum_{j=-l}^{l} F_l^j I_l^j(\mathbf{x} - \mathbf{x}_3), \tag{28}$$

where

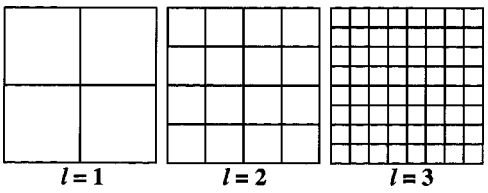

FIG. 2. Two-dimensional illustration of FMM hierarchical cell decomposition. At level l the MD cell is subdivided in each direction into 2^l cells.

$$F_l^j = \sum_{n=l}^{\infty} \sum_{m=-n}^{n} I_{n-l}^{m-j}(\mathbf{x}_3 - \mathbf{x}_2) E_n^m. \tag{29}$$

Equation (27) may now be used to compute the potential due to the charges in sphere S_0 at any point $\mathbf{x}$ that lies within the sphere S_3.

In the FMM the Coulomb potential is computed in a hierarchical manner. The MD cell is recursively divided in half along each of the Cartesian axes to obtain multiple sets of cells. This recursive decomposition is illustrated for the two-dimensional case in Fig. 2. In three dimensions the entire structure can be viewed as an octree data structure with the MD cell as the root of the tree, corresponding to level $l=0$. At each level in the tree there are 8^l number of cells (each parent in level $l-1$ produces eight children). The recursive decomposition continues to a level L at which point further refinements would make the cell size smaller than the cutoff distance for the short-range potentials. In other words, at the highest level of refinement each cell corresponds to a link cell in the link-cell list structure. Because the hierarchical decomposition in FMM is related to a tree structure, the cells at the highest level of refinement are often referred to as leaf cells. The FMM algorithm decomposes into two main procedures: the upward pass and the downward pass.

The upward pass starts at the highest level of refinement L by computing the outer multipoles C_n^m for each leaf cell (with respect to the center of the leaf cell) using (18). Since information about each atom is used only once, the computational cost is $O(Np^2)$, where p is the order of the multipole expansion. The outer multipoles D_l^j for each cell c in level L-1 are then computed from the outer multipoles C_n^m of c's children in level L by using the outer-to-outer transformation (25) to translate each child's outer multipoles to the parent's center and then they are added together. This procedure is repeated for each of the successive levels in the tree until level 2 is reached. Since the maximum number of possible leaf cells is N and each translation involves p^4 operations the computational cost is $O(Np^4)$. At the end of the upward pass the outer multipoles for all cells at all levels are determined.

Before describing the downward pass it is necessary to make a few definitions[30] that are illustrated for two dimensions in Fig. 3. At a level l the nearest neighbors of a cell c (dark cell in Fig. 3) are defined to be the set of 26 cells that share a boundary point with c (hatched cells in Fig. 3). Two cells are said to be well separated if they are separated by at least one cell. The *interaction set* for a cell c is defined to be the set of cells at the same level as c that are not nearest

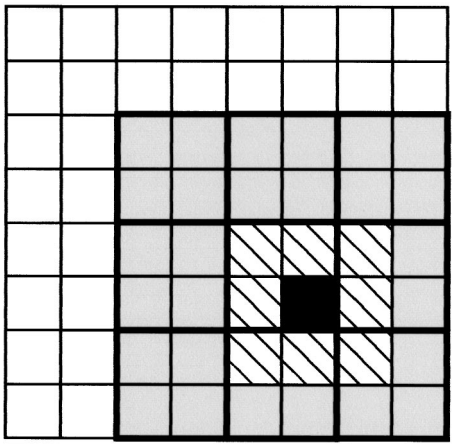

FIG. 3. Two-dimensional illustration of defined sets used in FMM. The hatched cells are the nearest neighbors of the dark cell. The *interaction set* for the dark cell is the set of shaded cells at the same level as the dark cell.

neighbors of c and whose parent cells are nearest neighbors of the parent of c (shaded cells in Fig. 3). Note that at any level there are at most 189 entries in the *interaction list* of a cell.

The downward pass operates by consistently computing interactions between cells at the coarsest level possible. This is accomplished for a given cell by computing interactions with those cells which are well separated and whose interactions have not been accounted for at the parent's level. The downward pass is initiated at the coarsest level by computing all the inner multipoles for each cell in the level. When free boundary conditions (no pbc) are used, the coarsest level that contains well separated cells is $l=2$. The inner multipoles for each cell c in the coarsest level are computed by converting the outer expansion of each cell that is well separated from c to an inner expansion about the center of c using the outer-to-inner translation (27), then adding them together. The downward pass then proceeds in a recursive manner, beginning at the next coarsest level, as follows.

(i) For each cell c in level l convert the inner expansion belonging to c's parent to an inner expansion about c's center using the inner-to-inner translation (29).

(ii) For each cell c in level l convert the outer expansion of each cell in c's *interaction list* to an inner expansion about c's center using the outer-to-inner translation (27) and then add them together.

(iii) Repeat steps (i) and (ii) for level $l+1$ until they are completed for all levels including the leaf-level L.

Once steps (i) and (ii) have been completed at the leaf level, the inner expansion for each leaf cell will contain the interactions with all other well-separated leaf cells. The number of operations required for steps (i) and (ii) is $\leqslant 190Np^4$. Finally, the far field contribution to the potential at each atomic position is computed from the inner expansion (28). This step requires $\leqslant Np^2$ operations. Altogether, the computation for the downward pass scales as Np^4.

The nearest neighbor leaf-cell contributions are computed directly using the link-cell lists with the number of operations proportional to N/N_b, where $N_b=N/8^L$ the average number of atoms per link cell. From the discussion of the upward pass, downward pass, and direct calculation it can be seen that the computational complexity of the FMM algorithm is $O(N)$. For realistic system sizes serial implementation can still be impractical, thus motivating the need for parallel computation.

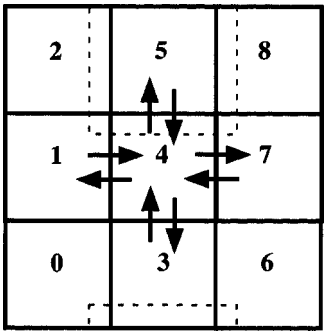

FIG. 4. Domain-decomposition scheme in two dimensions for nine nodes. Arrows indicate the direction of message passing. The dashed line indicates the copied boundary regions for node 5.

D. Parallel implementation of FMM with domain decomposition (Ref. 43)

We consider a system of N atoms contained within a unit MD cell. The partitioning of work among P processors (nodes) is accomplished via a divide-and-conquer strategy based on domain decomposition (see Fig. 4). The MD cell is subdivided into $P=P_x\times P_y\times P_z$ subsystems of equal volume. The nodes are logically arranged in an array such that a node p $(0\leqslant p\leqslant P-1)$ corresponds to the subsystem indexed by three integers[46]

$$p_x = \lfloor p/(P_y P_z) \rfloor$$

$$p_y = \lfloor p/P_z \rfloor \bmod P_y$$

$$p_z = p \bmod P_z \tag{30}$$

where $\lfloor x \rfloor$ denotes the greatest integer less than or equal to x. Figure 4 illustrates the domain decomposition for a two-dimensional system. All the attributes (coordinates, velocities, accelerations, species, etc.) associated with atoms located within a particular subsystem are stored within the memory of the corresponding node. The mapping of an atom's coordinates, $\mathbf{s}_i$, to a sequential node ID, $p(\mathbf{s}_i)$, is given by

$$p(\mathbf{s}_i) = p_x(\mathbf{s}_i)P_y P_z + p_y(\mathbf{s}_i)P_z + p_z(\mathbf{s}_i), \tag{31}$$

where

$$p_\alpha(\mathbf{s}_i) = \lfloor s_{i\alpha} P_\alpha \rfloor \quad (\alpha = x,y,z). \tag{32}$$

When atoms move out of a subsystem into a neighboring subsystem, the corresponding attributes (positions, velocities, etc.) are transferred using standard message-passing library routines.[47]

The calculation of short-range interatomic forces on atoms in a subsystem is done using the link-cell list scheme.

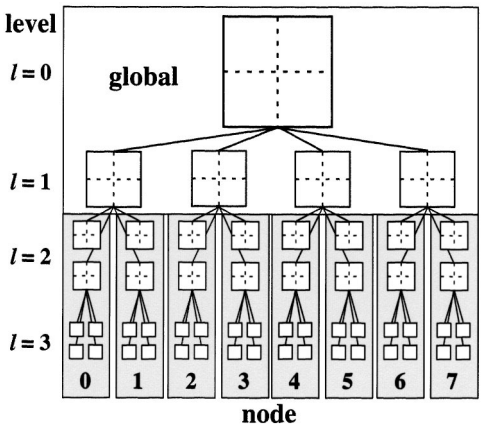

FIG. 5. Domain decomposition scheme for FMM in a two-dimensional system. In the lower levels, cells are local to a node. Cell information in the upper levels is made global to all nodes.

To calculate the forces on atoms within a subsystem, the coordinates of all the boundary atoms that reside in the 26 nearest-neighbor subsystems are required. The coordinates of boundary atoms are exchanged between nearest-neighbor nodes using *nonblocking* send and *blocking* receive operations. Newly received boundary atom coordinates are stored in augmented link-cell lists. Boundary-atom exchange between nearest neighbors is accomplished through six message-passing steps: north, south, east, west, upper, and lower. Boundary-atom coordinates that need to be exchanged with edge-sharing and corner-sharing neighbors are first passed to the appropriate face-sharing neighbor and then forwarded to the appropriate destination node during the subsequent message-passing steps. Newton's third law can be used to reduce the number of message-passing steps by a factor of 2. In this case, it is necessary to send the forces computed for boundary atoms back to the source node.

The unit MD cell is decomposed into $P=P_x\times P_y\times P_z$ subsystems with the requirement that each P_α be a power of 2. We define a level $L_g=\log_2[\max(P_x,P_y,P_z)]$ in the FMM tree. In the lower levels of the hierarchy, $l\geqslant L_g$, each cell is uniquely assigned to a node. For upper levels, $l<L_g$, the number of cells becomes smaller than the number of nodes. In this case, assignment of each cell to a node results in processors becoming idle. An alternative approach is to duplicate the multipole computations in the upper levels by setting the cells to be global. Figure 5 illustrates this decomposition scheme for a two-dimensional system.

In the parallel FMM implementation, the upward pass and downward pass proceed in a similar manner as in the serial case. The calculation of multipole expansions for the leaf cells according to Eq. (18) is local to each node. Because a parent cell and its children reside on the same node, the outer-to-outer translations of the upward pass and the inner-to-inner translations of the downward pass do not require any communication between nodes. To compute the outer-to-inner translations from a cell's interaction set, the outer multipoles of two boundary layer cells must be copied from the nearest-neighbor nodes. This is accomplished through message passing steps similar to that required for the short-range force calculations. The $8^l/P$ cells on a node are augmented with the copied outer multipoles to form an array consisting of the outer multipoles of $(2^l/P_x+2)(2^l/P_y+2)(2^l/P_z+2)$ cells at each layer. The outer-to-inner translations at each of the lower levels ($l\geqslant L_g$) are computed using the augmented set of outer multipoles. For upper levels ($l<L_g$) the global set of outer multipoles is used.

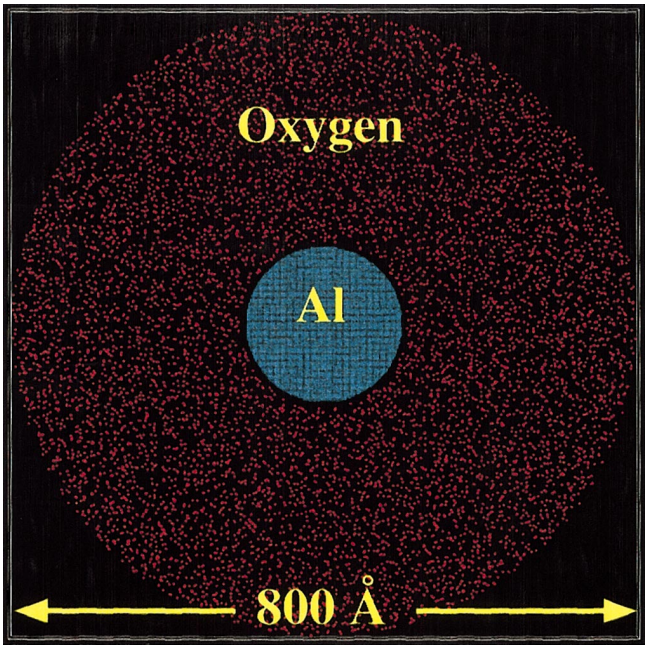

FIG. 6. (Color) Initial setup of oxidation simulation. This is an 8-Å-thick slice through the middle of the system. The aluminum cluster is cyan and the surrounding oxygen are red. A spherical reflecting wall of radius 400 Å contains the oxygen atoms.

E. Setup of oxidation simulations (Ref. 48)

The setup for the oxidation simulations is as follows (see Fig. 6). A fcc-crystalline Al sphere (diameter=200 Å) composed of 252,158 atoms and thermalized at 300 K is placed at the center of a cubic box of length 800 Å. A total of 530,720 oxygen atoms are distributed randomly outside the Al sphere (radius 110–400 Å) either in the form of atomic (O_1) or molecular (O_2) oxygen at a temperature of 300 K. The oxygen density is 40 times that of the normal state (1 atm and 300 K). A spherical reflecting wall of radius 400 Å confines the entire system. In order to accelerate computations, we use a multiple time step approach to compute short-range and long-range forces efficiently.[41] The equations of motion are integrated with $\Delta t=1$ fs for short-range forces and $\Delta t=20$ fs for long-range forces. New atomic charges are determined every 100 time steps such that the electrostatic energy is minimized subject to the constraint that the total system remains neutral. Canonical MD simulation, in which the temperature of the whole system is fixed at 400 K using Nosé-Hoover thermostat chain,[49] is performed for the case of O_2. In addition, microcanonical MD simulations are performed for both O_1 and O_2.

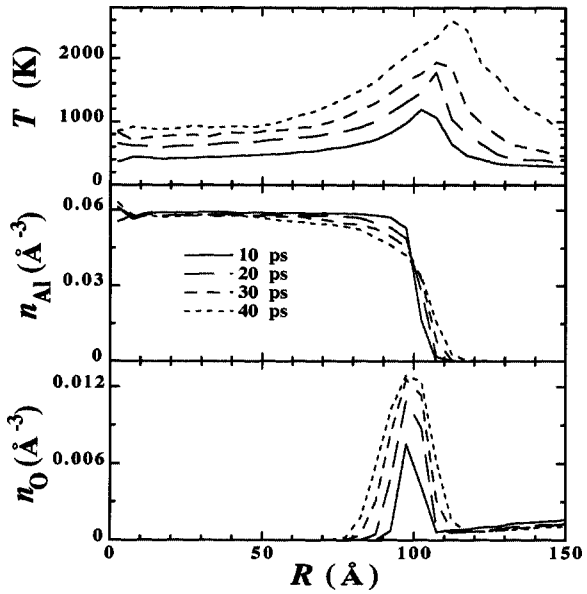

FIG. 7. Time evolution of temperature and density profiles as a function of distance from the center of the aluminum cluster for the O_2 microcanonical simulation.

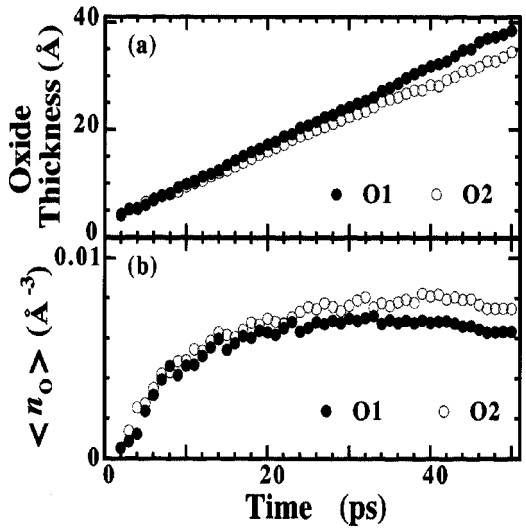

FIG. 8. (a) Thickness of oxide and (b) average density of oxygen in the oxide region as a function of simulation time in the O_1 and O_2 microcanonical simulations.

III. RESULTS

A. Explosive oxidation in the microcanonical ensemble

Recent experiments have demonstrated that small aluminum particles are highly explosive under high oxygen pressure and closed conditions.[50] Motivated by this experimental observation, we simulated the oxidation behavior in closed conditions without heat dissipation, i.e., the simulations were performed in the microcanonical ensemble performed for both atomic (O_1) and molecular (O_2) oxygen. Figure 7 shows a plot of the time evolution of temperature and density profiles in the O_2 microcanonical simulation as a function of distance from the center of the cluster. We observe that the energy released from Al-O bond formation leads to a dramatic increase in temperature in the surface region. Thermal energy is rapidly transported through the Al cluster, resulting in an average temperature of 1000 K in the core of the Al cluster (the melting temperature of Al is 933 K) by 40 ps. Rapid temperature increase in the reactive region (near surface) causes nanocluster to explode. Due to the increase in temperature, the density of aluminum atoms in the surface region drops and the cluster boundary increases to around 110 Å by 30 ps, see Fig. 7 (middle). Figure 7 (bottom) shows that oxygen atoms rapidly diffuse into the Al cluster, reaching a radius of 80 Å during the first 30 ps. The peak oxygen density increases rapidly during the first 30 ps and then saturates by 40 ps.

The rate of temperature increase at the nanocluster surface in the O_1 microcanonical simulation is 30% higher than that of the O_2 case. This difference is attributed to the energy required to dissociate the O_2 molecules before Al-O bonding occurs. Correspondingly, we observe that the rate of increase of the oxide layer thickness for the O_1 simulation is 13% larger than that of the O_2 simulation. This can be seen in Fig. 8(a) in which the oxide thickness as a function of simulation time is plotted for both the O_1 and O_2 cases. Thickness of the oxide region grows linearly with time without saturation during the simulation for both atomic (O_1) and molecular (O_2) oxygen cases. By 50 ps the thickness and temperature of the oxide region are 35 Å and 2500 K, respectively. In addition, the saturation density of oxygen in the nanocluster surface region for the O_1 simulation is 9% lower than that of the O_2 simulation, see Fig. 8(b).

Figure 9 shows the evolution of oxidation in a small slice (150 Å$\times$150 Å$\times$8 Å) of the O_2 microcanonical system at various times during the simulation. The charge transfer is localized to the surface region where the Al-O bonding occurs. Energy released from Al-O bond formation is rapidly transported through the cluster resulting in disordering of the Al crystal. Disordering of the Al crystal begins at the surface and moves rapidly inward as the temperature increases, resulting in an outward expansion of the oxide region. By 40 ps the thickness of the oxide scale is 22 Å and the temperature in the oxide region is 2000 K. Subsequently, we observe the ejection of small Al_xO_y fragments from the nanocluster surface, indicating that the nanocluster is exploding. This behavior under closed conditions has also been observed experimentally.[50] Similar behavior is observed in the O_1 microcanonical simulation, except that the O_2 dissociation energy lowers the rate of temperature increase at the nanocluster surface by 30%.

We have analyzed the evolution of local stresses during the oxidation process. Local stress distributions are conveniently calculated from[51]

$$\sigma_{\alpha\beta}^{\Omega} = \frac{1}{\Omega}\left\langle \sum_{i,\mathbf{r}_i\in\Omega} m_i v_i^{\alpha} v_i^{\beta} + \sum_{i,\mathbf{r}_i\in\Omega} \sum_{j>i} r_{ij}^{\alpha} f_{ij}^{\beta} \right\rangle \tag{33}$$

where α and β are Cartesian indices and the sum over i is restricted to atoms within a volume Ω.[52] The local stresses were calculated by subdividing the system into cells of length 10 Å and averaging the virial stress given in Eq. (33)

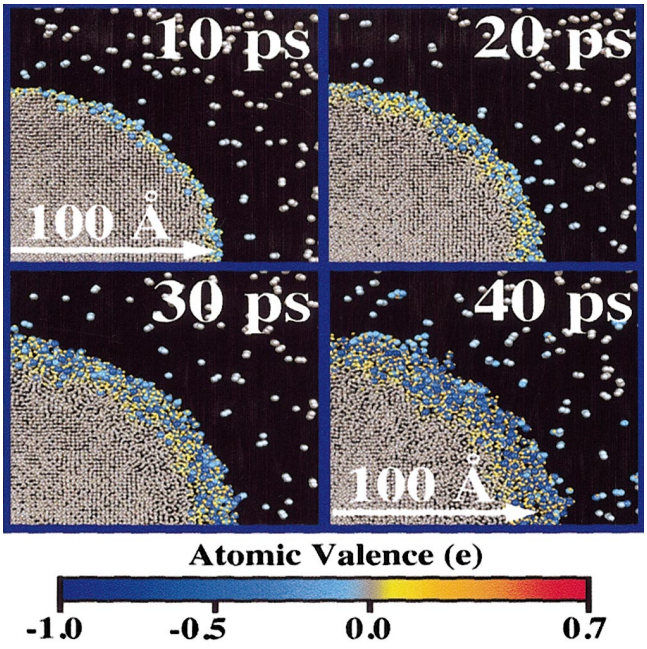

FIG. 9. (Color) Snapshots of a small slice (150 Å×150 Å ×8 Å) of the O_2 microcanonical system at various times during the simulation. The larger spheres correspond to oxygen and smaller spheres to aluminum; color represents the sign and magnitude of the charge on an atom.

in each cell over 1 ps intervals. We observe large transient stress gradients followed by equilibration as the oxidation progresses. Figure 10 depicts the time evolution of local pressure in the nanocluster for the O_1 microcanonical simulation. Initially, the surface region is tensile, while the inner region of the cluster is at zero pressure. We attribute the tensile stress in the surface region to the strong Coulomb forces created by the charge transfer between the surface Al atoms and the incoming O atoms. Heat transfer from the surface to the inner region then causes the pressure in the inner region to become compressive. Subsequently, the pressure differences between the surface and interior regions equilibrate.

The local stress regions are further examined by separating the contributions from the electrostatic and nonelectrostatic forces. Figure 11 depicts the electrostatic and nonelectrostatic force contributions to the local pressure after 100 ps. It can be seen from Fig. 11(a) that the attractive Coulomb force between aluminum and oxygen contributes a large negative pressure localized in the oxide. The electrostatic pressure contribution increases in magnitude toward the middle of the oxide where charge transfer is the highest. The large attractive forces are partially offset by steric repulsion which gives rise to a positive nonelectrostatic contribution to the local pressure in the oxide, see Fig. 11(b). Analysis of local stresses reveals large stress gradients throughout the nanocluster with the oxide largely under negative pressure and the metal core under positive pressure. Local pressures range between −1 and 1 GPa. The local stresses were calculated by averaging the atomic virial in 6-Å voxels over a 1-ps interval.

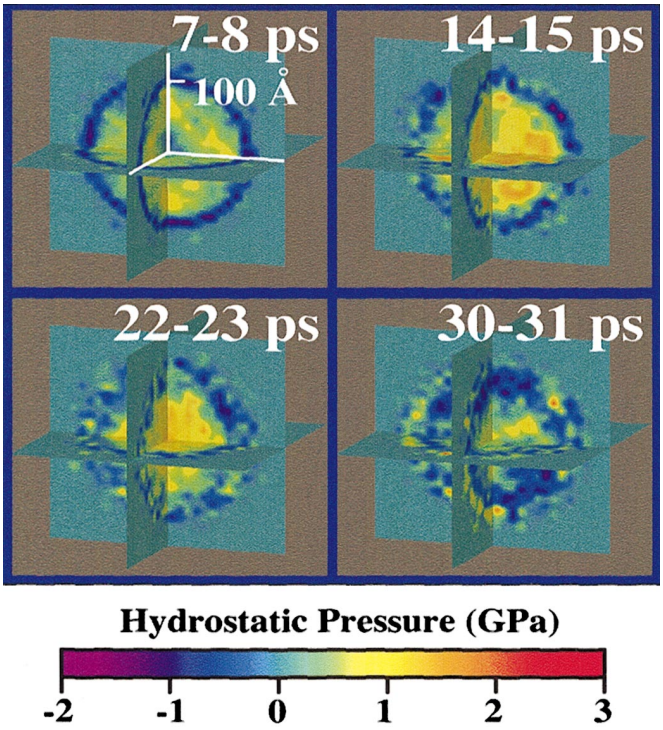

FIG. 10. (Color) Three-dimensional views of local pressures in the O_1 microcanonical simulation. The system is subdivided into 10 Å cells and the virial stress in each cell is averaged over 1 ps intervals.

B. Formation of oxide scale in the canonical ensemble

In addition to the microcanonical simulations we have investigated the oxidation process in the O_2 environment in the canonical ensemble. Figure 12 shows the oxide thickness as a function of simulation time for the first 260 ps of the O_2 canonical simulation. Kinetic analysis of the oxidation process reveals two different oxide-scale regimes. In the initial stage, for the first 50 ps, we observe that the oxide thickness increases linearly with time to 25 Å, subsequently the rate becomes smaller and the thickness saturates at 33 Å. The

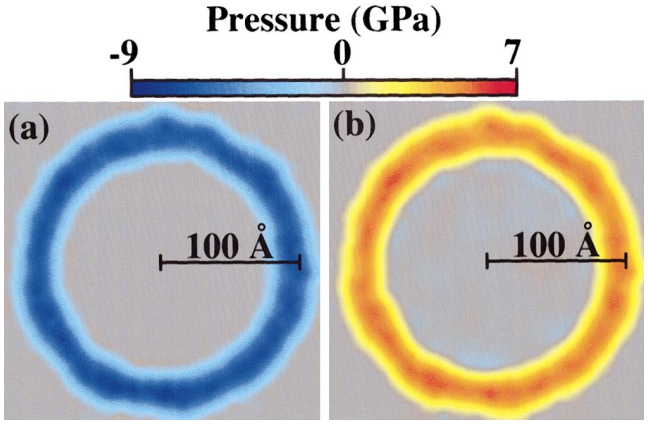

FIG. 11. (Color) (a) Electrostatic and (b) nonelectrostatic contributions to the local pressure in the nanocluster after 100 ps of simulation time.

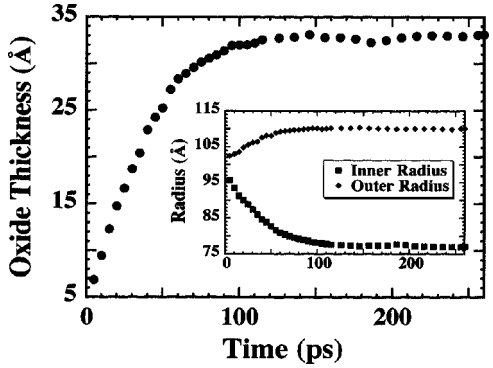

FIG. 12. Thickness of oxide layer as a function of simulation time for the O_2 canonical simulation. The inner and outer radial extent of the oxide layer as a function of simulation time are shown in the inset.

inset for Fig. 12 shows the inner and outer radial extent of the oxide. The growth of the oxide scale is both inward and outward: inward because of the movement of oxygen towards the interior of the cluster and outward because of the movement of aluminum towards the oxide surface. The inward and outward growth of the oxide saturate at 77 and 110 Å, respectively, with the inward growth saturating later than the outward. Therefore, the inward diffusion of oxygen atoms (23 Å) is greater than the outward diffusion of aluminum atoms (10 Å) along the developing oxide scale. This is in agreement with experimental observations.[22]

During the first 100 ps the temperature in the oxide region increases to 1500 K, near the melting temperature of alumina, where it subsequently remains. The large stress gradients give rise to diffusion of atoms in the oxide region. Analysis of the atomic diffusivities in the oxide show that during the first 100 ps the diffusivity of aluminum is 30%–60% larger than that of oxygen. This is due to the smaller steric size of aluminum. We calculate diffusivities from mean-square displacements computed over a 1-ps interval. At 50 ps the diffusivities of aluminum and oxygen are 1.4×10^{-4} and 1.1×10^{-4} cm^2/s, respectively. By 100 ps the diffusivity of oxygen has dropped to 7.4×10^{-5} cm^2/s, while that of aluminum only decreases to 1.2×10^{-4} cm^2/s. The radial and tangential diffusivities remain about equal, indicating that while the oxide grows radially, high tangential diffusion causes uniformity in the oxide thickness with respect to polar angles.

Saturation of the oxide growth during the first 260 ps is accompanied by a depletion of oxygen outside the nanocluster. In order to bring the oxide as close as possible to complete saturation, we continue the O_2 simulation in the canonical ensemble to 466 ps while maintaining n_O outside the nanocluster in the range 0.001–0.002 $Å^{-3}$. An oxide scale of 40 Å thickness is subsequently formed, as seen in Fig. 13, which is a snapshot of a small slice (115 Å×115 Å×8 Å) of the system at 466 ps. The outer radial extent of the oxide remains at 110 Å; however, the inner radial extent moves to 70 Å. The average mass density of the oxide is 2.9 g/cm^3 ($n_{Al}=0.042$ $Å^{-3}$ and $n_O=0.038$ $Å^{-3}$), which is about 75% of the crystalline α-Al_2O_3 density. Significant charge transfer is observed in the oxide region, as can be seen from Fig. 13

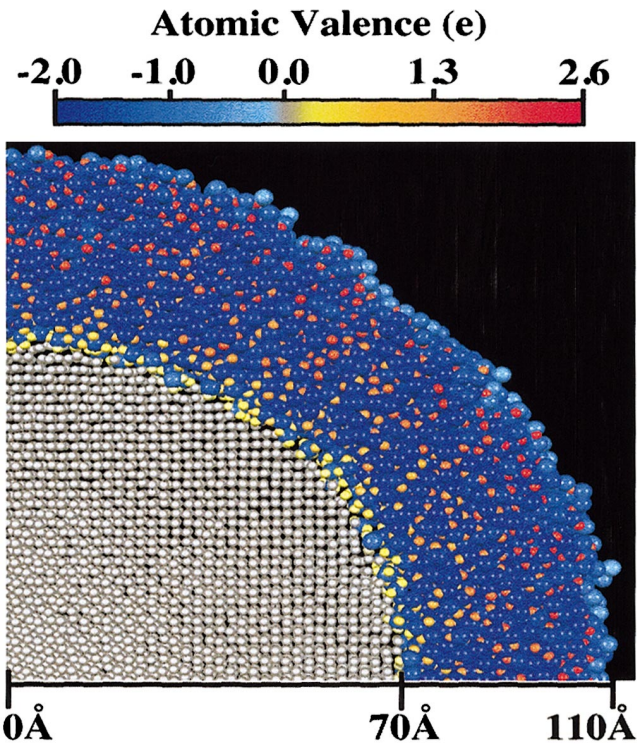

FIG. 13. (Color) Snapshot of a small slice (150 Å×150 Å ×8 Å) of the O_2 canonical system after 466 ps of simulation time. The larger spheres correspond to oxygen and smaller spheres to aluminum; color represents the sign and magnitude of the charge on an atom.

where color represents the sign and magnitude of the charge on an atom. Maximum and average atomic charges in the oxide region are, respectively, 2.6*e* and 1.7*e* for Al and −2.0*e* and −1.8*e* for O. Charge transfer in the oxide is significant and decreases in magnitude near the interfaces.

Aluminum nanoclusters of diameters 100–700 Å are known to form oxide scales of thickness 20–50 Å in low-density oxygen gases at room temperature.[7,16,17] The thickness of oxide scales as a function of cluster size for small aluminum clusters have been measured.[16] For Al clusters of diameter 200 Å the thickness is 30–40 Å. Despite orders of magnitude difference in the oxygen-gas densities, remarkable similarity in the oxide thickness is found between the present simulation results and the experimental observations.

Experimentally, the structure of the oxide scale on Al nanoclusters is not fully known and is considered to be amorphous. However, in all of the known literature there is no detailed structural analysis of the oxide scale on Al nanoclusters. Recent studies have pointed out that the local structure of the amorphous oxide scale for Al nanoclusters is different from the amorphous scale that forms on the bulk Al surface.[7,14,15] However, details of the differences between the two amorphous oxides are not known.

We analyze structural correlations in the oxide region through partial pair-distribution functions, coordination numbers, and bond-angle distributions. Figure 14(a) shows the Al-O pair-distribution function for three spherical shells in the oxide region. These results show a variation of structures as we pass through the oxide from the metal-oxide interface

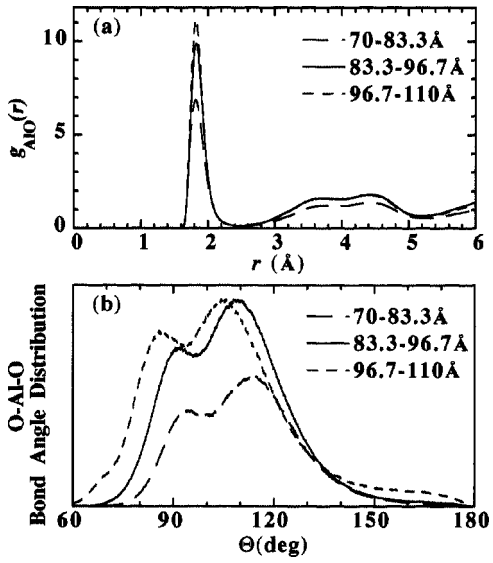

FIG. 14. Structural correlations in three spherical shells of the oxide layer at $t=466$ ps. (a) Al-O pair-distribution functions. (b) O-Al-O bond angle distributions.

(70–83.3 Å) to the oxide interior (83.3–96.7 Å) and on to the oxide-environment interface (96.7–110 Å). In Fig. 14(a) we observe that the position of the $g_{\mathrm{AlO}}(r)$ peak gives the Al-O bond length to be around 1.81 Å in the metal-oxide region. The position of the Al-O peak remains nearly constant for larger r in the interior and oxide-environment regions. Pair distributions for Al-Al and O-O show shifts in the peak positions related to the change in the relative Al and O densities in each region. The corresponding coordination numbers for Al in each region [obtained by integrating $g_{\mathrm{AlO}}(r)$ up to 2.5 Å] are 3.1 for the metal-oxide interface, 3.9 in the interior of the oxide region, and 4.3 for the oxide-environment interface.

Figure 14(b) shows the O-Al-O bond-angle distribution for each region in the oxide. We see that throughout the oxide region there are two distinct peaks in the bond-angle distribution. In the interior of the oxide the distribution shows two peaks at 90° and 109°. These peaks shift toward smaller angles in the oxide-environment interface, reflecting the decrease in aluminum density. In the metal-oxide interface where the oxygen density is lower, we observe that the peaks in the bond-angle distribution shift toward larger angles.

It is interesting to compare the present results with those for liquid alumina, which is made up of tetrahedrally coordinated aluminum,[53] and amorphous alumina formed by anodization, which consists of a mixture of tetrahedrally and octahedrally coordinated aluminum.[54,55] Additionally, aluminum ions in porous alumina films are known to be predominately tetrahedrally (or even lower) coordinated.[55] Reported Al-O bond lengths in amorphous Al_2O_3 films range from 1.8 to 1.9 Å, depending on the porosity and method of preparation.[55] The stoichiometry of the oxide region in the current simulation is different from that of Al_2O_3, and consequently its structural correlations are rather different from those in liquid and amorphous Al_2O_3. Despite the presence of two peaks around 90° and 109° in the bond-angle distribution in Fig. 14(b), which might suggest the coexistence of octahedrally and tetrahedrally coordinated Al atoms, we find that Al atoms in the oxide region are predominantly four coordinated, which indicates significant distortion of the structural units.

C. Oxidative percolation in the canonical ensemble

We have found in Fig. 12 that the growth rate of the oxide thickness in the canonical run begins to decrease at around 30 ps. Through detailed analyses of trajectories O atoms and of their formation of OAl_n structures, we propose here a three-step process in the early stage of oxidation of the Al nanoparticle, to explain such a decrease in the oxidation rate.

Step 1. The first 5 ps

After the simulation starts, O_2 molecules near the nanoparticle surface are attracted toward the surface. We monitor trajectories of the O_2 molecules after they approach the nanoparticle surface, and find that the molecules dissociate into two O atoms on the surface and the two O atoms enter into either the octahedral or the tetrahedral site of the fcc Al. Figure 15 shows a small portion of the nanoparticle surface at 2.5 ps to depict an example of such events. In Fig. 15, surface Al atoms are drawn with small spheres, while O atoms with large spheres; color attached to an atom represents the charge number obtained through the variable-charge calculation. White lines are drawn in Fig. 15 to indicate a fcc unit (deformed). Two green curves in Fig. 15 depict trajectories of two O atoms, which demonstrate that one O atom goes into the octahedral site and the other into the tetrahedral site. Charges of the two O atoms in Fig. 15 are both about $-0.2|e|$. Both the tetrahedron (OAl_4) and the octahedron (OAl_6) clusters are nearly charge neutral; $-0.03|e|$ and $0.05|e|$, respectively.

Step 2. Between 5 and 25 ps

The O atoms diffuse through the tetrahedral and the octahedral sites of the fcc Al due to their high velocities corresponding to about 2×10^3 K. We evaluate residence times of the O atoms and find significant variations of them as the simulation progresses. Figure 16 shows the residence times of the O atoms at the tetrahedral and the octahedral sites, as functions of the nanoparticle radius and the simulation time. To create Fig. 16, we first partition the nanoparticle into 2.5 Å depth radial shells, calculate the residence times of the O atoms, and then average the times over the atoms in each shell for every 5 ps. At the simulation time $\sim$5 ps, maximum values of the residence times at the tetrahedral and the octahedral sites are both about 0.8 ps. As the simulation progresses, however, the maximum residence time at the tetrahedral site increases toward 1.2 ps, while that at the octahedral site decreases to 0.2 ps. An increased degree of relative stability of tetrahedrally coordinated OAl_4 clusters becomes apparent at around 20 ps. In this connection, we note that the ground state of alumina, i.e., α-Al_2O_3, may be regarded as edge and corner sharing OAl_4 clusters.

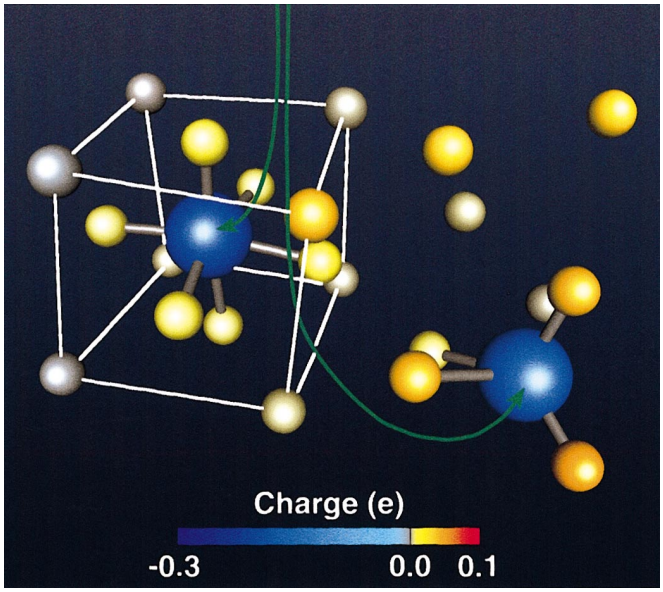

FIG. 15. (Color) A small portion of the surface of the nanoparticle at 2.5 ps in the canonical simulation. Trajectories of two O atoms forming an O_2 molecule at the initial, are drawn with green curves. Al atoms are depicted with small spheres, and O atoms with large spheres. Color represents the atomic charge obtained in the variable-charge calculation.

Step 3. Between 25 and 35 ps

The tetrahedral clusters (OAl_4) coalesce by either corner or edge sharing Al atoms to form a percolating network enclosing the nanoparticle. Such a percolation behavior is demonstrated in Fig. 17. To draw the figure, we first select O atoms forming OAl_4 clusters. Those clusters sharing one or more Al atoms are regarded as mutually connected. Connecting clusters with the cluster size $N_s > 50$ are plotted in Fig. 17 at 20, 27, 30, and 31 ps. In between 30 and 31 ps, a percolating network of the clusters is formed, enclosing the nanoparticle. Charge density of the surface oxide (see Fig. 7) is as small as 0.04–0.05 $Å^{-3}$ during 20–35 ps. This neutral tetrahedral network may decelerate the diffusion of O into and the diffusion of Al out of the nanoparticle, and hence, result in a decrease in the oxidation rate.

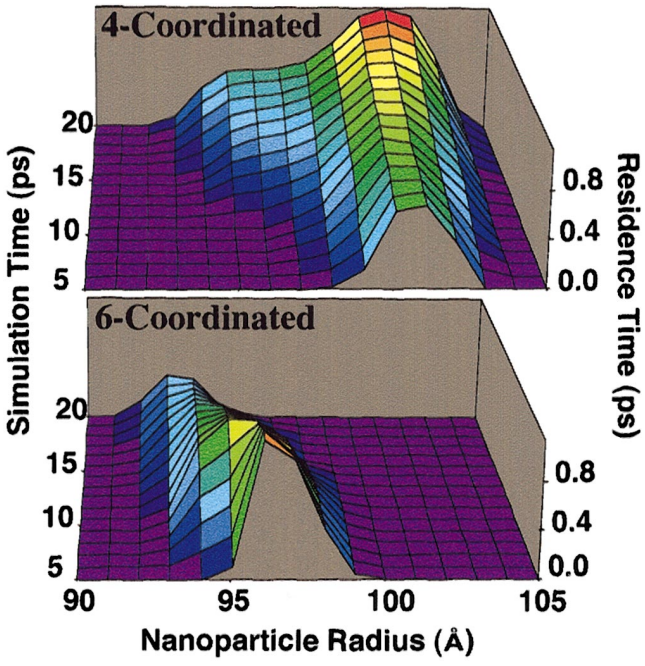

FIG. 16. (Color) Residence times of the O atoms at the tetrahedral (four-coordinated) and the octahedral (six-coordinated) sites, as functions of the nanoparticle radius and the simulation time in the canonical simulation.

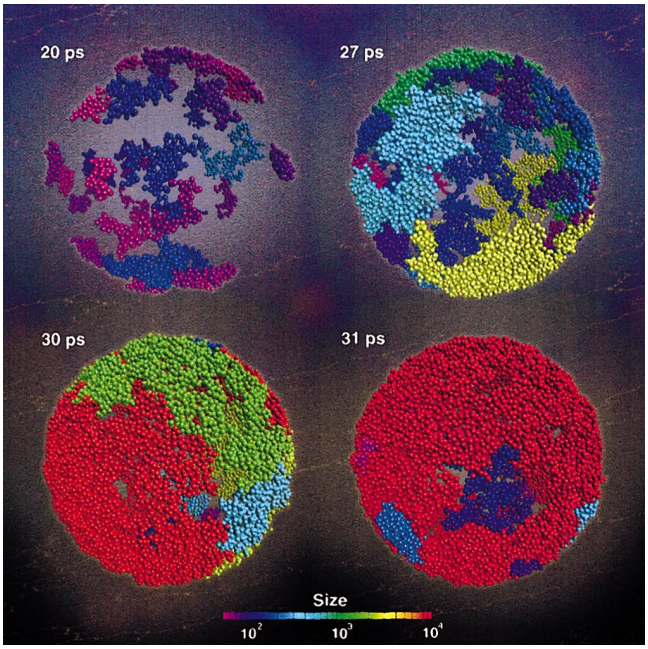

FIG. 17. (Color) Tetrahedrally coordinated O atoms with the cluster size $N_s > 50$ are drawn at 20, 27, 30, and 31 ps in the canonical simulation. Color represents N_s.

IV. CONCLUSION

In conclusion, we have performed large-scale MD simulations on parallel computers to study the oxidation of an aluminum nanocluster of radius 100 Å. The simulations take into account the effect of charge transfer between Al and O based on the electronegativity equalization principle. We have employed the $O(N)$ fast multipole method to compute the Coulomb interaction arising from charge transfer. Simulations have been carried out for both microcanonical and canonical ensembles and for atomic and molecular oxygen environments. In the microcanonical ensemble, simulations with atomic and molecular oxygen show a continuous increase in the thickness and average temperature of the oxide layer with time. Subsequently, melting (exploding) of the nanocluster is observed in both settings, with the atomic case occurring earlier than in the molecular case due to the dissociation energy of the O_2 molecule. In the canonical simulations, a passivating amorphous oxide scale with a thickness of 4 nm and an average mass density of 2.9 g/cm^3 is formed during 466 ps of simulation time. The calculated oxide thick-

ness is in good agreement with experimental results on aluminum clusters of sizes similar to that used in the simulations. The average mass density in the oxide region is 75% of the crystalline alumina density. During the oxide growth, large pressure variations occur that result in rapid diffusion of atoms in the oxide. The large negative pressure contribution from electrostatic forces in the oxide is partially offset by the positive contribution of steric repulsion. This results in the oxide remaining largely under negative pressure, which causes aluminum to diffuse toward the surface and oxygen to diffuse towards the interior of the cluster. The diffusivity of aluminum is 30–60 % higher than that of oxygen in the oxide. Owing to variations in Al and O densities, structures in the oxide scale vary when passing through the oxide from the metal-oxide interface to the oxide-environment interface. Significant charge transfer is observed in the reactive region (oxide scale) in the microcanonical and canonical simulation. Through detailed analyses of trajectories and their microscopic structures, we have found a three-step process of oxidative percolation that explains deceleration of oxide growth at the early stage of the canonical simulation. These atomistic mechanisms could complement recent theoretical results on oxidation based on *ab initio* electronic structure calculations.[56]

This work was supported by ARO-MURI: Penn State-USC-U Illinois-Urbana, DARPA_PROM, DOE and NSF. Simulations were performed at the Department of Defense's Major Shared Resource Centers under CHSSI and Challenge projects, USC HPC Center, and parallel computing facilities of the Collaboratory for Advanced Computing and Simulations.

[1] J. Karch, R. Birringer, and H. Gleiter, Nature (London) **330**, 556 (1987).
[2] H. Gleiter, Prog. Mater. Sci. **33**, 223 (1989).
[3] R. W. Siegel, in *Materials Interfaces: Atomic-Level Structure and Properties*, edited by D. Wolf and S. Yip (Chapman Hall, London, 1992), p. 431.
[4] H. Gleiter, Nanostruct. Mater. **1**, 1 (1992).
[5] A. Pechenik, G. J. Piermarini, and S. C. Danforth, J. Am. Ceram. Soc. **75**, 3283 (1992).
[6] R. W. Siegel, Mater. Sci. Eng., A **168**, 189 (1993).
[7] T. G. Nieh, P. Luo, W. Nellis, D. Lesuer, and D. Benson, Acta Mater. **44**, 3781 (1996).
[8] R. W. Siegel, J. Phys. Chem. Solids **55**, 1097 (1994).
[9] R. W. Siegel and G. E. Fougere, Nanostruct. Mater. **6**, 205 (1995).
[10] K. Tsuruta, A. Omeltchenko, R. K. Kalia, and P. Vashishta, Europhys. Lett. **33**, 441 (1996).
[11] R. K. Kalia, A. Nakano, K. Tsuruta, and P. Vashishta, Phys. Rev. Lett. **78**, 689 (1997).
[12] R. K. Kalia, A. Nakano, A. Omeltchenko, K. Tsuruta, and P. Vashishta, Phys. Rev. Lett. **78**, 2144 (1997).
[13] J. C. Sánchez-López, A. Fernández, C. F. Conde, A. Conde, C. Moraat, and J. M. Sanz, Nanostruct. Mater. **7**, 813 (1996).
[14] J. C. Sánchez-López, A. R. González-Elipe, and A. Fernández, J. Mater. Res. **13**, 703 (1998).
[15] B. H. Suits, P. Apte, D. E. Wilken, and R. W. Siegel, Nanostruct. Mater. **6**, 609 (1995).
[16] S. Sako, K. Ohshima, and T. Fujita, J. Phys. Soc. Jpn. **59**, 662 (1990).
[17] C. E. Aumann, G. L. Skofronick, and J. A. Martin, J. Vac. Sci. Technol. B **13**, 1178 (1995).
[18] C. Wagner, Z. Phys. Chem. Abt. B **21**, 25 (1933).
[19] N. F. Mott, Trans. Faraday Soc. **35**, 1175 (1939).
[20] N. Cabrera and N. F. Mott, Rep. Prog. Phys. **12**, 163 (1948–49).
[21] D. R. Askeland, *The Science and Engineering of Metals*, 2nd ed. (CPWS-KENT, Boston, 1989), Sec. 20-8.
[22] A. Atkinson, Rev. Mod. Phys. **57**, 437 (1985).
[23] F. H. Streitz and J. W. Mintmire, Phys. Rev. B **50**, 11996 (1994).
[24] S. Nosé, Mol. Phys. **52**, 255 (1984).
[25] S. Nosé, J. Chem. Phys. **81**, 511 (1984).
[26] W. G. Hoover, Phys. Rev. A **31**, 1695 (1985).
[27] G. J. Martyna, M. L. Klein, and M. Tuckerman, J. Chem. Phys. **97**, 2635 (1992).
[28] M. W. Finnis and J. E. Sinclair, Philos. Mag. A **50**, 45 (1984).
[29] R. P. Iczkowski and J. L. Margrave, J. Am. Chem. Soc. **83**, 3547 (1961).
[30] A. K. Rappé and W. A. Goddard, J. Phys. Chem. **95**, 3358 (1991).
[31] C. C. J. Roothaan, J. Chem. Phys. **19**, 1445 (1951).
[32] L. Greengard, *The Rapid Evaluation of Potential Fields in Particle Systems* (MIT Press, Cambridge, MA, 1987).
[33] W. J. Mortier, K. Van Genechten, and J. Gasteiger, J. Am. Chem. Soc. **107**, 829 (1985).
[34] W. J. Mortier, S. K. Ghosh, and S. Shankar, J. Am. Chem. Soc. **108**, 4315 (1986).
[35] S. W. Rick, S. J. Stuart, and B. J. Berne, J. Chem. Phys. **101**, 6141 (1994).
[36] S. Ogata, H. Iyetomi, K. Tsuruta, F. Shimojo, R. K. Kalia, A. Nakano, and P. Vashishta, J. Appl. Phys. **86**, 3036 (1999).
[37] S. Ogata, H. Iyetomi, K. Tsuruta, F. Shimojo, R. K. Kalia, A. Nakano, and P. Vashishta, Mater. Res. Soc. Symp. Proc. **581**, 667 (2000).
[38] S. Ogata, H. Iyetomi, K. Tsuruta, F. Shimojo, R. K. Kalia, A. Nakano, and P. Vashishta, J. Appl. Phys. **88**, 6011 (2000).
[39] G. H. Golub and C. F. Van Loan, *Matrix Computations*, 3rd ed. (Johns Hopkins University Press, Baltimore, 1996).
[40] A. Nakano, Comput. Phys. Commun. **104**, 59 (1997).
[41] M. Tuckerman, B. J. Berne, and G. L. Martyna, J. Chem. Phys. **97**, 1990 (1992).
[42] L. Greengard and V. Rokhlin, J. Comput. Phys. **73**, 325 (1987).
[43] S. Ogata, T. J. Campbell, R. K. Kalia, A. Nakano, P. Vashishta, and S. Vemparalac, Comput. Phys. Commun. **153**, 445 (2003).
[44] J. D. Jackson, *Classical Electrodynamics*, 2nd ed. (Wiley, New York, 1975).
[45] M. A. Epton and B. Dembart, SIAM J. Sci. Comput. (USA) **16**, 865 (1994).
[46] D. C. Rapaport, Comput. Phys. Commun. **62**, 217 (1991).
[47] M. Snir, S. W. Otto, S. Huss-Lederman, D. W. Walker, and J.

Dongara, *MPI: The Complete Reference* (MIT Press, Cambridge, MA, 1996).
[48] T. J. Campbell, R. K. Kalia, A. Nakano, P. Vashishta, S. Ogata, and S. Rodgers, Phys. Rev. Lett. **82**, 4866 (1999).
[49] G. J. Martyna, M. Tuckerman, D. J. Tobias, and M. L. Klein, Mol. Phys. **87**(5), 1117 (1996).
[50] The explosive nature of aluminum under high oxygen pressure and closed conditions has been observed at NASA Lewis [Ali Sayir (private communication)].
[51] W. G. Hoover, *Molecular Dynamics* (Springer-Verlag, Berlin, 1986).
[52] J. F. Lutsko, J. Appl. Phys. **64**, 1152 (1989).
[53] S. Ansell, S. Krishnan, J. K. Richard Weber, J. J. Felten, P. C. Nordine, M. A. Beno, and D. L. Price, Phys. Rev. Lett. **78**, 464 (1997).
[54] A. J. Bourdillon, R. G. Jones, and A. J. Forty, Philos. Mag. A **49**, 341 (1984).
[55] I. Levin and D. Brandon, J. Am. Ceram. Soc. **81**, 1995 (1998).
[56] M. Todorova, W. X. Li, M. V. Ganduglia-Pirovano, C. Stampfl, K. Reuter, and M. Scheffler, Phys. Rev. Lett. **89**, 096103 (2002).